



# Raw sugarcane juice assisted hybrid electrolysis for formic acid and hydrogen production based on reversible redox cycle of CoNi LDH

Yunpeng Liu<sup>a,b</sup>, Zhongxin Chen<sup>c</sup>, Yunyi Yang<sup>b</sup>, Ren Zou<sup>b</sup>, Binglu Deng<sup>a</sup>, Linxin Zhong<sup>b</sup>, Kian Ping Loh<sup>c</sup>, Xinwen Peng<sup>b,\*</sup>

<sup>a</sup> School of Materials Science and Hydrogen Energy, Foshan University, Foshan 528231, PR China

<sup>b</sup> State Key Laboratory of Pulp and Paper Engineering, South China University of Technology, Guangzhou 510641, PR China

<sup>c</sup> Department of Chemistry, National University of Singapore, 3 Science Drive 3, 117543, Singapore

## ARTICLE INFO

### Keywords:

Hybrid electrolysis  
Sucrose oxidation  
Solar-driven device  
Raw sugarcane juice  
Hydrogen production

## ABSTRACT

The major bottleneck in self-powered water splitting devices by renewable energy lies in the kinetically sluggish oxygen evolution reaction (OER), which only produces low-value oxygen. Herein, we explore sucrose electro-oxidation as an alternative anodic reaction for production of valuable chemicals at a reduced electricity consumption. By developing a reversible redox cycle of  $\text{Ni}^{2+}/\text{Ni}^{3+}$  and  $\text{Co}^{2+}/\text{Co}^{3+}$  in the CoNi layered double hydroxide (LDH), the required voltage of sucrose oxidation for  $100 \text{ mA cm}^{-2}$  is reduced by 240 mV compared to oxygen evolution. The sucrose electrooxidation by CoNi LDH is a two-step reaction including the electro-oxidation of  $\text{Ni}^{2+}/\text{Co}^{2+}$  to  $\text{Ni}^{3+}/\text{Co}^{3+}$  and the spontaneous reaction between  $\text{Ni}^{3+}/\text{Co}^{3+}$  and sucrose. By feeding with natural sugarcane juice, a solar-driven electrolyser is assembled for the co-production of value-added formic acid and hydrogen. Our work demonstrates a sustainable route for integrating hydrogen production and biomass electrooxidation for energy applications.

## 1. Introduction

Compared with the steam reforming of fossil fuels, the water electrolysis driven by renewable resource-derived electricity has considered as a promising technology for scalable green hydrogen production [1–3]. Unfortunately, the anodic oxygen evolution reaction (OER) severely limits the efficiency of such devices [4], which requires a much higher voltage than theoretical value to compensate its sluggish multiple electron transfer kinetics [5]. The anodic product, oxygen, is a product with little interest and presents a possible explosion hazard in the gas mixture with hydrogen [6]. This urges an energy-efficient and sustainable alternative for industrially viable water electrolysis technology. For instance, chemical-assisted water electrolysis is a practical strategy to reduce the electricity consumption [7–9]. The electrooxidation of organics is thermodynamically and kinetically more favorable than OER, thus lowering the full cell voltage for hydrogen production [10–12]. This is accompanied with a profitable co-production of value-added chemicals at anode to further mitigate the energy cost.

Among various hybrid systems, biomass oxidation coupled with hydrogen evolution reaction (HER) is of particular interest [13–16]. The

biomass upgrading via electrooxidation is an attractive alternative to fossil fuels, which presents a potential role for value-added chemicals and fuels production. Recently, Shi et al. reported an HER and glycerol oxidation hybrid electrolysis system for paired production of  $\text{H}_2$  and value-added formate using the Ni-Mo-N/CFC bifunctional catalyst. The coupled system only required a low cell voltage of 1.36 V at  $10 \text{ mA cm}^{-2}$ , which was 260 mV lower than that of water splitting [17]. The hybrid water electrolysis has considered as a promising technology for renewable energy supply. Although proven to be practical, the use of purified chemical as feed inevitably increases the production cost of hydrogen. A more preferable configuration for hybrid system involves feeding of raw biomass [18]. For instance, sugarcane, an important cash crop counting for approximately 80 % of global sugar production [19]. The raw sugarcane juice is a potential substance for hybrid electrolysis, providing a simplified alternative for existing biofuel production via fermentation [20,21]. Electrocatalytic upgrading of its major fragment, i.e., sucrose oxidation reaction (SOR) is thereby superior to other similar biomass oxidations, owing to its high conversion and selectivity, simple separation of products, and mild reaction conditions. The hybrid electrolysis can not only maximize the return of energy investment, but also

\* Corresponding author.

E-mail address: [fexwpeng@scut.edu.cn](mailto:fexwpeng@scut.edu.cn) (X. Peng).

<https://doi.org/10.1016/j.apcatb.2023.122559>

Received 22 September 2022; Received in revised form 14 January 2023; Accepted 1 March 2023

Available online 9 March 2023

0926-3373/© 2023 Elsevier B.V. All rights reserved.

demonstrates an effective pathway in biomass upgrading.

Herein, we demonstrate a solar-driven hybrid electrolyser using raw sugarcane juice as feed, by coupling the SOR with HER for co-production of value-added formic acid (FA) and green hydrogen. Scheme 1 shows the blueprint for sustainable energy conversion integrating with sugarcane valorization by hybrid electrolysis. By inventing a CoNi layered double hydroxide (LDH) with reversible redox cycle of  $\text{Ni}^{2+}/\text{Ni}^{3+}$  and  $\text{Co}^{2+}/\text{Co}^{3+}$  as the anodic catalyst for SOR, we can afford a current density of  $100 \text{ mA cm}^{-2}$  at only  $1.36 \text{ V}$  versus reversible hydrogen electrode (vs. RHE). A series of characterization methods reveal that the  $\text{Ni}^{2+}/\text{Co}^{2+}$  are electrochemically oxidized into  $\text{Ni}^{3+}/\text{Co}^{3+}$ , then the formed  $\text{Ni}^{3+}/\text{Co}^{3+}$  are reduced by sucrose, hence completing the reversible redox cycle. This work paves the way toward sustainable production of hydrogen and biofuels for solution of the energy and environment crisis.

## 2. Experimental section

### 2.1. Materials

All the chemicals were purchased from Aladdin and used without further purification including potassium hydroxide (KOH, 95 %), sucrose (99 %), fructose (98 %), glucose (98 %), methanol (99.9 %), cobalt chloride hexahydrate ( $\text{CoCl}_2 \cdot 6 \text{ H}_2\text{O}$ , 99 %), nickel nitrate hexahydrate ( $\text{Ni}(\text{NO}_3)_2 \cdot 6 \text{ H}_2\text{O}$ , 99 %), cetyltrimethyl ammonium bromide (CTAB, 99 %), sodium hypophosphite monohydrate ( $\text{NaH}_2\text{PO}_2 \cdot \text{H}_2\text{O}$ , 99 %). And the sugarcane juice was extracted from fresh sugarcane (Guangzhou).

### 2.2. Synthesis of CoNi LDH on Ni foam

The CoNi LDH electrocatalyst on the Ni foam was prepared by hydrothermal method. The Ni foam was first sequentially cleaned by  $1 \text{ M}$  HCl, acetone, deionized water and ethyl alcohol using an ultrasonic bath cleaner. Then the Ni foam ( $1 \times 3 \text{ cm}^2$ ) was immersed into a  $50 \text{ mL}$  Teflon-lined autoclave with a homogeneous solution containing  $\text{CoCl}_2 \cdot 6 \text{ H}_2\text{O}$  ( $0.4 \text{ mmol}$ ),  $\text{Ni}(\text{NO}_3)_2 \cdot 6 \text{ H}_2\text{O}$  ( $0.2 \text{ mmol}$ ), CTAB ( $500 \text{ mg}$ ),  $\text{H}_2\text{O}$  ( $3 \text{ mL}$ ), and methanol ( $15.2 \text{ mL}$ ), followed by heating in an oven at  $140^\circ\text{C}$  for  $18 \text{ h}$  to allow the growth of CoNi LDH nanosheets on Ni foam. The Ni foam covered with CoNi LDH nanosheets was washed by deionized water and ethanol, and then dried at  $60^\circ\text{C}$  for  $12 \text{ h}$ . The

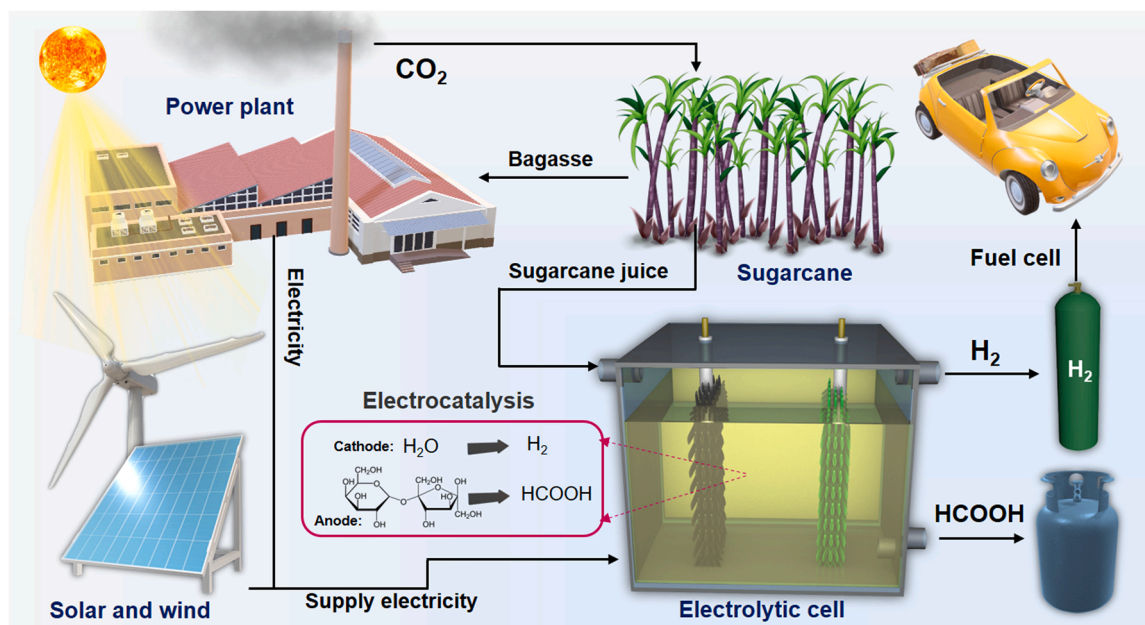
loading of CoNi LDH on Ni foam was calculated by acid dissolution method. The prepared electrode was placed in  $1 \text{ M}$  HCl and ultrasonically cleaned for  $1 \text{ min}$  to completely remove the CoNi LDH. The sample was weighed after washing and drying. The mass difference before and after dissolution was the loading mass of CoNi LDH, which was calculated to be  $2090 \mu\text{g cm}^{-2}$ .

### 2.3. Synthesis of CoNiP<sub>x</sub> on Ni foam

The as-prepared CoNi LDH on Ni foam was transferred to a clean porcelain crucible. Subsequently,  $500 \text{ mg}$  of  $\text{NaH}_2\text{PO}_2 \cdot \text{H}_2\text{O}$  was directly covered on the Ni foam, followed by calcining in a tubular furnace at  $350^\circ\text{C}$  for  $2.5 \text{ h}$  under the  $\text{N}_2$  atmosphere, at a heating rate of  $2^\circ\text{C min}^{-1}$  [22]. Finally, the obtained sample was washed with distilled water and ethanol, and then dried in a  $60^\circ\text{C}$  for  $8 \text{ h}$ . The CoNi LDH was converted to  $\text{Ni}_x\text{P}_y$  and  $\text{CoP}_2$ , and the obtained sample was labeled as CoNiP<sub>x</sub>.

### 2.4. Characterizations

Scanning electron microscope (SEM) was performed using a Hitachi SU5000 equipped with a field emission gun. Field emission transmission electron microscope (TEM) was collected using a JEOL JEM-2100 F. X-ray photoelectron spectroscopy (XPS) analyses were performed using Thermo ESCALAB 250 with  $\text{Al K}\alpha$  X-ray, and the energy correction was calibrated by referencing the  $\text{C } 1\text{s}$  peak of adventitious carbon to  $284.8 \text{ eV}$ . X-ray powder diffraction (XRD) was conducted using Bruker D8 Advance X-ray diffractometer with  $\text{Cu K}\alpha$  radiation. The metal content was measured by Inductively coupled plasma-optical emission spectrometry (ICP-OES, Agilent 720ES). Elemental analysis was acquired by Elementar Vario EL cube. The contents of sucrose, glucose, and fructose in sugarcane juice were measured by ion chromatograph (Thermo ICS5000, Thermo Scientific, US) equipped with a CarboPac™ PA1 column ( $250 \times 4.0 \text{ mm}$ ), and  $100 \text{ mM}$  NaOH aqueous solution was used as the eluent at  $30^\circ\text{C}$  with a flow rate of  $1.0 \text{ mL/min}$ . Raman spectra were collected using a confocal Raman microscope (Horiba LabRAM HR Evolution) with an excitation wavelength of  $532 \text{ nm}$  and a  $50 \times$  objective. The *in situ* Raman spectra were recorded with Pt wire as counter electrode and  $\text{Ag}/\text{AgCl}$  as reference electrode. An average of three measurements of Raman spectrum was collected over a collection



**Scheme 1.** The sustainable pathways for co-production hydrogen and formic acid products by sugarcane-fed hybrid water electrolysis.

time of 30 s. Raman frequencies were calibrated using a Si wafer.

## 2.5. Electrocatalytic measurements

All the electrochemical experiments were acquired by the CHI 760E electrochemical workstation under a three-electrode configuration, using Ag/AgCl (saturated KCl) as the reference electrode. The acquired potentials were quoted with respect to the reversible hydrogen electrode (RHE) through  $V \text{ (vs. RHE)} = V \text{ (vs. Ag/AgCl)} + 0.197 + 0.0591 \times \text{pH}$ . The HER and OER were conducted in 1.0 M of  $\text{H}_2$ - or  $\text{O}_2$ -saturated KOH electrolytes (pH = 13.9, measured by pH meter). Before the electro-oxidation test, fresh electrocatalyst was activated by repetitive LSV until a stable OER performance was obtained. The electrooxidation reaction was performed in 1.0 M KOH electrolyte in the presence of 50 mM sucrose. The stability of CoNi LDH electrocatalyst was evaluated by chronoamperometry in three consecutive cycles. The scan rate of linear sweep voltammetry (LSV) was set to  $2 \text{ mV s}^{-1}$ , and all the LSV and chronoamperometry tests were recorded with continuous stirring. The two-electrode electrolysis was performed using CoNi LDH as anode,  $\text{CoNiP}_x$  as cathode, and 1.0 M KOH with sugarcane juice as electrolyte. The  $\text{CoNiP}_x$  cathode prepared by phosphating treatment of CoNi LDH showed a high HER performance, which was an ideal alternative to Pt noble metal cathode. Electrochemical impedance spectroscopy (EIS) tests were performed in the frequency range of  $10^5 \text{ Hz}$  to  $10^{-1} \text{ Hz}$  under

an applied bias ranging from 1.20 to 1.65 V (vs. RHE). In order to present valid iR compensation and to avoid excessive correction, iR compensation of 85 % instead of 100 % was applied to all the electrochemical experiments. Faradaic efficiency of products was calculated by equation: Faradaic efficiency (%) =  $(n_e \times n \times F) / Q \times 100 \%$ , where  $n_e$  is the number of electrons exchanged;  $n$  is the mol of products;  $F$  is the Faraday's constant ( $96,485 \text{ C mol}^{-1}$ );  $Q$  is the total charge. Solar driven proton exchange membrane (PEM) electrolysis was constructed using sugarcane juice as fuel. A H-type electrochemical cell was connected to a commercial solar panel (maximum power of 3 W, 6 V) through a slide rheostat (0–5 Ohm). An ampere meter was used to obtain the real-time current value in the circuit. The CoNi LDH and  $\text{CoNiP}_x$  were served as anode and cathode, respectively. The anolyte was 1.0 M KOH with sugarcane juice, while the catholyte was 1.0 M KOH. The  $\text{H}_2$  and  $\text{O}_2$  gases were collected and measured by water drainage method in 1 h reaction.

## 2.6. Product detection

Liquid products of selective oxidation were analyzed by high-performance liquid chromatography (HPLC, Agilent 1260 series) equipped with a UV detector at 210 nm and a Bio-Rad Aminex HPX-87 H column ( $300 \text{ mm} \times 7.8 \text{ mm} \times 9 \mu\text{m}$ ). 5 mM  $\text{H}_2\text{SO}_4$  was used as the mobile phase at  $35^\circ\text{C}$  with a flow rate of 0.6 mL/min. The

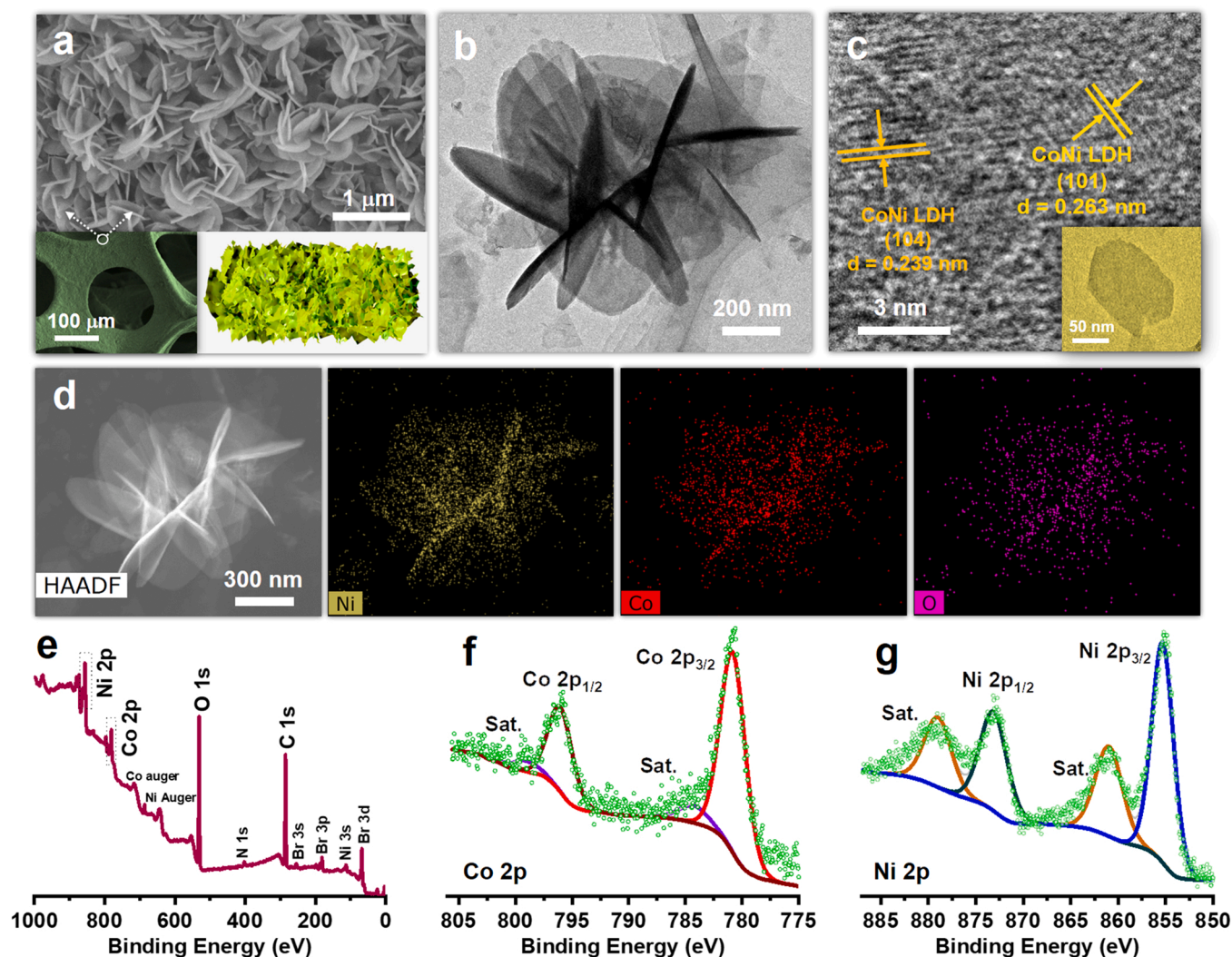


**Fig. 1.** (a) SEM images of the CoNi LDH on Ni foam. (b) TEM image of CoNi LDH nanoflower. (c) HR-TEM image of CoNi LDH, inset shows the CoNi LDH nanosheet. (d) HAADF-STEM and the corresponding elemental mappings. XPS spectra of (e) broad scan, (f) Co 2p, (g) Ni 2p of the CoNi LDH.



concentrations of the liquid products were determined by the calibration curve established with the external standards. Hydrogen and oxygen were analyzed by a gas chromatograph (GC-9790II, Fuli, China) equipped with the thermal conductivity detector (TCD) and the 5 A molecular sieve column ( $\Phi 3 \text{ mm} \times 1 \text{ m}$ ).

### 3. Results and discussion

#### 3.1. Synthesis and structural characterization

Three-dimensional (3D) CoNi LDH nanoflowers were grown on Ni foam via a facile hydrothermal process with cetyltrimethyl ammonium bromide (CTAB) as the additive. Such 3D interconnected arrays are composed of petaloid nanoflowers with smooth surface in the scanning electron microscopy (SEM), as shown in Fig. 1a and Fig. S1. Transmission electron microscope (TEM) image in Fig. 1b indicates that the nanoflower is composed of ultrathin nanosheets with thickness of around 6 nm (Fig. S2). Such an intersected structure provides abundant active sites with facilitated charge transport and diffusion kinetics in the electrochemical reaction [23]. The parallel lattice fringes of 0.239 nm and 0.263 nm in high-resolution TEM (HR-TEM) correspond to the (104) and (101) planes of CoNi LDH, respectively (Fig. 1c) [24]. Uniform distribution of the Ni, Co, and O elements throughout the nanoflower is confirmed by energy-dispersive X-ray spectroscopy (EDS) elemental mapping (Fig. 1d), demonstrating the formation of CoNi LDH. The existence of Br in nanoflowers is derived from CTAB during hydrothermal synthesis of CoNi LDH (Fig. S3).

Owing to strong interference of Ni foam, the CoNi LDH was prepared without Ni foam for X-ray diffraction (XRD) analysis. Typical diffraction peaks of CoNi LDH at  $11.3^\circ$ ,  $22.4^\circ$ ,  $34.4^\circ$ ,  $38.8^\circ$ ,  $60.0^\circ$  and  $61.2^\circ$  are observed in Fig. S4, in good agreement with the (003), (006), (012), (015), (110) and (113) facets of hydrotalcite-like LDH phase, respectively [25–27]. The composition and chemical state of CoNi LDH were analyzed by X-ray photoelectron spectroscopy (XPS). Apart from the Co, Ni and O elements, the Br element is also detected in CoNi LDH. The Br

ions from CTAB were absorbed on the CoNi LDH during synthesis (Fig. 1e). High resolution XPS spectrum of Co 2p in Fig. 1f reveals a doublet at binding energies of 780.8 and 796.0 eV for the  $2p_{3/2}$  and  $2p_{1/2}$  of  $\text{Co}^{2+}$ , respectively [28,29]. Two weak satellite (Sat.) peaks of Co 2p located at 784.4 and 799.1 eV are also observed. Similarly, the Ni 2p XPS spectrum in Fig. 1g evidences the presence of  $\text{Ni}^{2+}$ , with binding energies located at 855.3 for Ni  $2p_{3/2}$  and 873.1 eV for Ni  $2p_{1/2}$  [27], respectively. O 1s peak with binding energies at 530.8 eV and 532.2 eV in Fig. S5 are attributed to the hydroxyl groups in LDH and water molecules adsorbed on surface [30]. The Co/Ni atomic ratio in CoNi LDH determined by ICP-OES is 1:1.6 (Table S1). The oxygen mass fraction in CoNi LDH tested by elemental analysis is 38 %. Hence, the above results confirm the successful synthesis of CoNi LDH, and the intersected nanoflowers arrays endow the electrode with large current density in electrochemical process.

#### 3.2. Electrocatalytic performances for sucrose oxidation

As-prepared CoNi LDH was used as the anode for sucrose oxidation in a three-electrode setup with an Ag/AgCl reference electrode and a Pt foil counter electrode. Fig. 2a shows the linear sweep voltammetry (LSV) curves of CoNi LDH in 1.0 M KOH with or without the addition of 50 mM sucrose. In the absence of sucrose, a voltage of 1.60 V (vs. RHE) is required to afford a current density of  $100 \text{ mA cm}^{-2}$  for OER. The apparent peak centered at 1.38 V is attributed to the oxidation peaks of  $\text{Ni}^{2+}/\text{Ni}^{3+}$  and  $\text{Co}^{2+}/\text{Co}^{3+}$  [31,32]. In presence of sucrose, the current density significantly increases due to SOR, leading to a striking reduction in overpotential to 1.36 V at  $100 \text{ mA cm}^{-2}$ . Such difference (240 mV) indicates that SOR is kinetically and thermodynamically more favorable than OER [33]. The effect of Fe contamination from the KOH electrolyte on SOR and OER is discussed in Fig. S6. The current density of OER preformed in 1.0 M KOH electrolyte with Fe purification slightly decreases, indicating that the trace amounts of Fe in KOH will affect the OER performance of CoNi LDH. However, the similar LSV curve of CoNi LDH for SOR in Fe-free KOH indicates that the trace amounts of Fe have

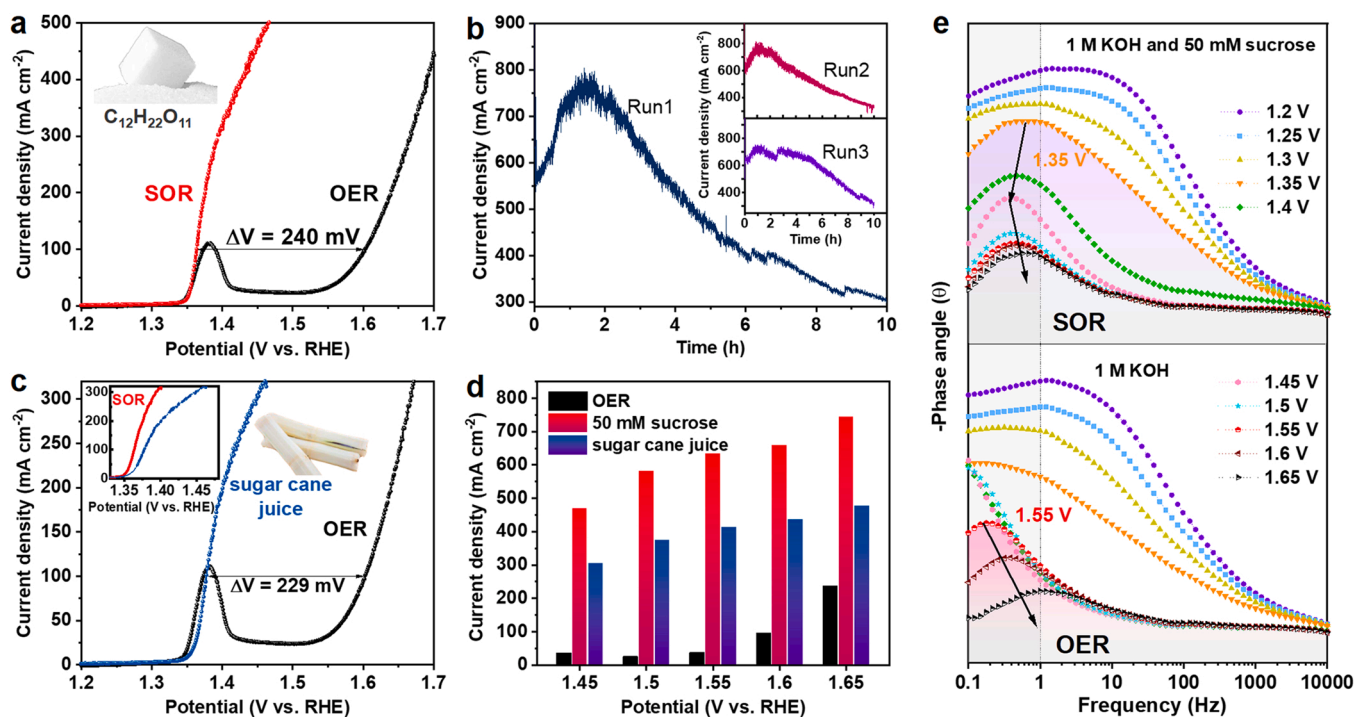


Fig. 2. (a) LSV curves of the CoNi LDH in the presence or absence of 50 mM sucrose. (b) Consecutive three 10 h-runs of sucrose oxidation at 1.6 V (vs. RHE). (c) Electrochemical performance using raw sugarcane juice and (d) the corresponding current densities at various potentials. (e) Bode plots of the CoNi LDH electrode for SOR and OER at different potentials.

little influence on SOR performance. As shown in Fig. S7, the activity of CoNi LDH toward SOR is concentration dependent. The optimal concentration is 50 mM of sucrose, where further concentration increase has little effect. At 1.45, 1.5, 1.55, 1.6, and 1.65 V (vs. RHE), current density of SOR markedly rise to 470.4, 581.2, 633.2, 658.8 and 743.2 mA cm<sup>-2</sup>, respectively (Fig. S8). In addition, CoNi LDH displays significantly higher SOR and OER performances than that of Ni foam (Fig. S9). The steady-state Tafel slopes of SOR and OER were constructed by sampling current density after 100 s of chronoamperometry at various potentials and correcting for iR compensation of 100 % (Fig. S10) [34]. The uncompensated resistance was tested by electrochemical impedance spectroscopy (EIS), which was 3.6 and 2.4 Ω in 1.0 M KOH with and without 50 mM sucrose, respectively. The CoNi LDH shows a rather low Tafel slope of 34.43 mV dec<sup>-1</sup> for the SOR, which is much lower than that of OER (125.36 mV dec<sup>-1</sup>), indicating much faster catalytic kinetics and higher transfer coefficient of SOR. The chronoamperometry at 1.6 V (vs. RHE) in Fig. 2b exhibits gradually decreased current density due to consumption of sucrose and change of pH value caused by the FA product. The same phenomenon occurs in chronoamperometry tested at 1.45 V (vs. RHE) (Fig. S11). The activity can be recovered by refreshing new electrolyte in three consecutive scans, demonstrating the excellent stability and reusability of CoNi LDH for sucrose oxidation. The halide ions from reagent were introduced into the catalyst system during synthesis. The effect of halide ions on SOR is discussed in Fig. S12. LSV curves of CoNi LDH for SOR in the presence of 50 mM KBr or KCl indicate that the halide ions have little influence on SOR performance.

Product analysis was performed by gas chromatography (GC) and high-performance liquid chromatography (HPLC). The H<sub>2</sub> production agrees well with theoretical values for an almost 100 % Faradaic efficiency (FE) for HER (Fig. S13). Particularly, no oxygen is produced, suggesting that Faradaic efficiency of O<sub>2</sub> at 1.6 V (vs. RHE) is 0 % (Fig. S14). The liquid products were determined by liquid chromatography via the calibration curve for 5 h (Fig. S15). Further analysis by HPLC on the liquid products reveals an extremely high selectivity (> 96 %) toward FA at different potentials, together with small amounts of lactic acid and trace amount of acetic acid (Figs. S16–S17), demonstrating a high activity and selectivity towards anodic sucrose oxidation. The SOR is the dominant process in anodic reaction, with almost 100 % Faradaic efficiency at different potentials.

The reaction mechanism of SOR on the CoNi LDH electrode was investigated. Time-dependent HPLC results in Fig. S18 indicate that an initial formation of glucose and fructose via SOR, and subsequent oxidation of monosaccharides into FA along the reaction progress. This is verified by electrochemical oxidation of glucose and fructose monomer in Fig. S19. The monosaccharides oxidation show the lower onset potential than that of SOR, which require a low potential of 1.3 (glucose) and 1.32 V (fructose) to achieve a current density of 100 mA cm<sup>-2</sup> (Fig. S20). Proposed mechanism of sucrose electrooxidation is depicted in Fig. S21. It is confirmed that the occurrence of pyranose-ring opening and glycosidic bond breaking reactions at lower Gibbs free energies than that of water splitting [35,36], agreeing well with the electrochemical test results.

To further extend the practicability of our hybrid electrolysis, raw sugarcane juice from fresh sugarcane (Guangzhou) was fed to the system as a replacement of sucrose. The sugar content in sugarcane juice was determined by ion chromatography as 340.18, 23.67, and 80.17 mM for sucrose, glucose and fructose, respectively (Tables S2–S3). The sugarcane juice was diluted at the factor of 2, 5, 10, 20, and 40, and then adding KOH to the solution until the concentration of KOH stayed at 1 M (Fig. S22). As expected, the activity is also concentration dependent when using sugarcane juice as electrolyte (Fig. S23), where the optimal dilution factor of 10 provides a similar current density and onset potential to SOR (inset of Fig. 2c). The required voltage to reach a current density of 100 mA cm<sup>-2</sup> is significantly reduced by 229 mV compared to OER, as shown in Fig. 2c. The reduced potential of sugarcane juice

oxidation is very close to SOR, indicating the feasibility and sustainability of sugarcane juice oxidation electrolysis. Fig. 2d shows a more detailed comparison in OER, SOR and sugarcane juice oxidation. Remarkable increase in current densities to 304.3, 373.9, 413.6, 437.6 and 477.6 mA cm<sup>-2</sup> are observed for sugarcane juice oxidation at 1.45, 1.5, 1.55, 1.6, and 1.65 V. HPLC analysis in Fig. S24 validates that the FA is the major product (88.7 % selectivity) when using chronoamperometry at a potential of 1.6 V (vs. RHE) for 5 h. Due to the complexity of raw sugarcane, a small amount of LA and trivial acetic acid (AA) are also detected. The possible CO<sub>2</sub> production during the SOR was checked by limewater (Fig. S25), and the results indicated that no CO<sub>2</sub> was produced during the SOR. In consideration of the influence of Pt foil counter electrode in electrochemical measurement of Pt-free catalysts, the SOR and OER performance using a graphite counter electrode are shown in Fig. S26a. The Pt counter electrode has little effect on electrochemical performance of CoNi LDH. Furthermore, the system using Pt as foil working electrode has almost no SOR and OER performances (Fig. S26b).

### 3.3. Insights into the role of Ni<sup>2+</sup>/Ni<sup>3+</sup> and Co<sup>2+</sup>/Co<sup>3+</sup> redox cycle in sucrose oxidation

To establish the structure–activity relationship, electrochemical impedance spectroscopy (EIS) was employed to probe the reaction interface during the OER or SOR process. *In-situ* Bode phase plots were observed in Fig. 2e. The peaks in high frequency region (10<sup>-1</sup>–10<sup>0</sup> Hz) should be assigned to the oxidation of the electrode inner [37,38]. The oxidation of CoNi LDH electrocatalysts occur in both the SOR and OER processes before the reactions begin. The peaks in low-frequency region (10<sup>0</sup>–10<sup>5</sup> Hz) is related to the nonhomogeneous charge distribution, namely the formation of oxidation species on the electrode interface [10]. A transition peak found at the potential of 1.55 V (vs. RHE) suggests the occurrence of OER, which is consistent with its OER onset potential. In the presence of sucrose, a much earlier transition peak is found at the potential of 1.35 V, indicating the high activity of SOR. The transition peaks of SOR first move to low frequency and then to high frequency, different from that of OER. It is because that the oxidation of Ni<sup>2+</sup>/Co<sup>2+</sup> to Ni<sup>3+</sup>/Co<sup>3+</sup> and the sucrose oxidation reaction proceed at the same time at the potential of 1.35–1.4 V. The Co<sup>3+</sup>/Ni<sup>3+</sup> (CoOOH and NiOOH) is the active intermediate for both the sucrose and water oxidation.

Controlled multi-potential chronoamperometry was conducted to investigate the in-depth correlation between the interface reaction of CoNi LDH electrode and subsequent oxidation of sucrose. Firstly, a high potential of 1.5 V was set for the oxidation of Ni<sup>2+</sup> and Co<sup>2+</sup> (M<sup>2+</sup>) into Ni<sup>3+</sup> and Co<sup>3+</sup> (M<sup>3+</sup>) in 1 M KOH (Fig. 3a). After switching the potential to 1.1 V, a cathodic current was observed owing to the electrochemical reduction of M<sup>3+</sup> into M<sup>2+</sup>. In contrast, the cathodic current disappeared when the sucrose was injected during the open circuit state (Fig. 3b). The M<sup>3+</sup> were reduced into M<sup>2+</sup> spontaneously by sucrose without external potential, thus resulting in the disappearance of reduction current. The same phenomenon occurred when the sucrose was present from the beginning (Fig. 3c), the high anodic current at 1.5 V was due to the sucrose oxidation. Furthermore, the cyclic voltammetry curves of CoNi LDH for SOR and OER are shown in Fig. S27a. The OER of CoNi LDH exhibits obvious oxidation and reduction peaks of Co and Ni. However, the reduction peak distinctly diminishes in intensity, owing to the reaction between sucrose and Co<sup>3+</sup>/Ni<sup>3+</sup>. During the negative scan of SOR, the oxidation current from 1.35 to 1.30 V is also owing to the sucrose oxidation (Fig. S27b). From above, we conclude that the M<sup>2+</sup> is first electrooxidized into M<sup>3+</sup> during the sucrose oxidation, and then recovered to initial state by spontaneous and immediate reduction by sucrose, furnishing a highly reversible redox cycle of Ni<sup>2+</sup>/Ni<sup>3+</sup> and Co<sup>2+</sup>/Co<sup>3+</sup> (Fig. 3d) [39].

*In-situ* Raman measurements were performed to monitor the structural evolution of the CoNi LDH during electrocatalytic process. In the

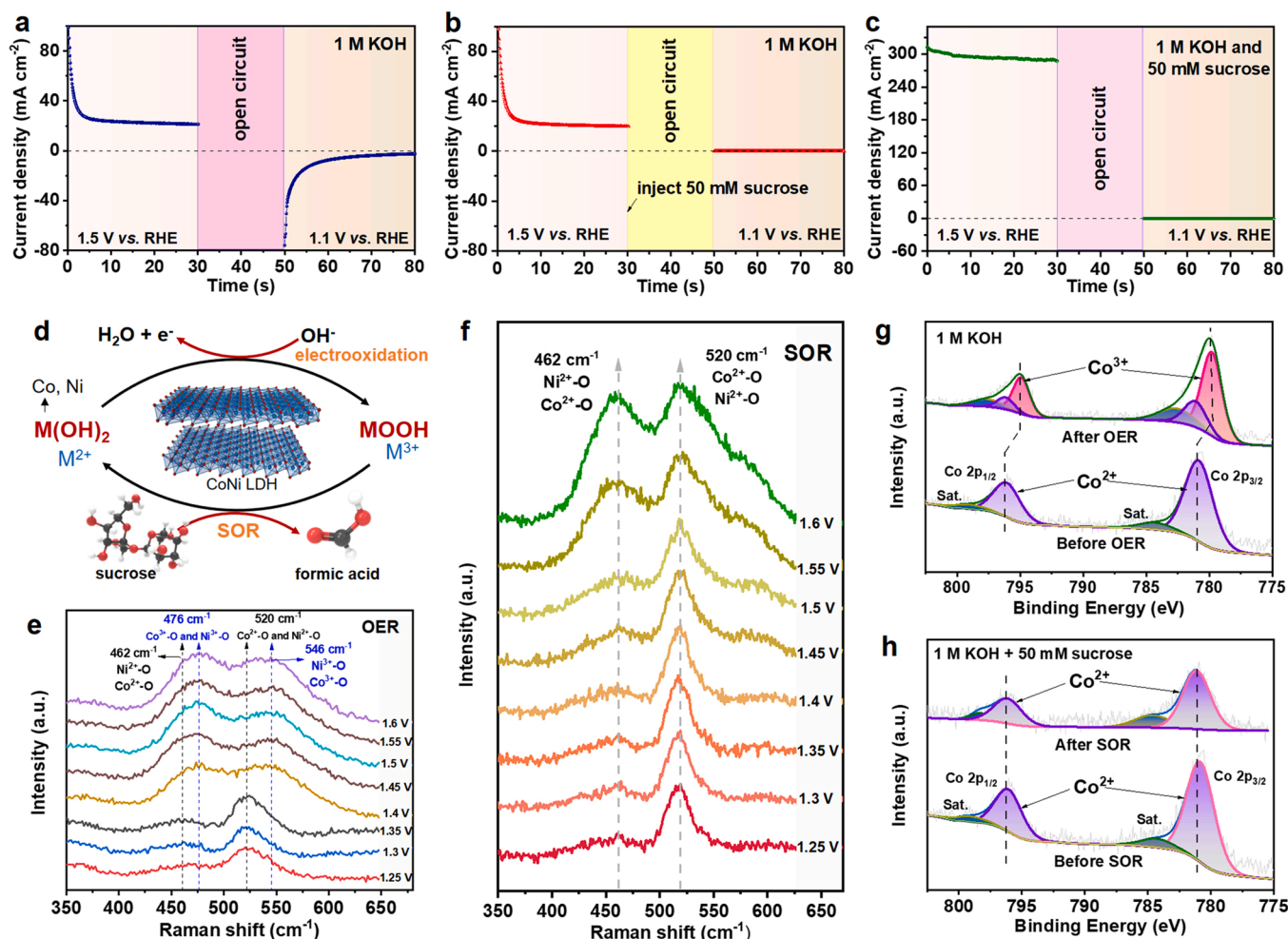


**Fig. 3.** Multi-potential chronoamperometry of CoNi LDH electrode in various conditions: (a) in 1 M KOH, (b) in 1 M KOH (injecting 50 mM sucrose during open circuit time), and (c) in 1 M KOH and 50 mM sucrose. (d) Schematic of the reversible redox cycle of  $\text{Ni}^{2+}/\text{Ni}^{3+}$  and  $\text{Co}^{2+}/\text{Co}^{3+}$  during SOR. *In-situ* Raman spectra of CoNi LDH for (e) OER and (f) SOR. XPS spectra of CoNi LDH before and after the electrochemical reaction: (g) in 1 M KOH and (h) in 1 M KOH with 50 mM sucrose.

absence of sucrose, two peaks located at  $462$  and  $520\text{ cm}^{-1}$  are assigned to the vibrations of  $\text{Ni}^{2+}\text{-O}$  and  $\text{Co}^{2+}\text{-O}$  in  $\text{Ni}(\text{OH})_2$  and  $\text{Co}(\text{OH})_2$  at  $1.25\text{ V}$  (vs. RHE) in KOH (Fig. 3e) [40,41]. After  $1.40\text{ V}$ , two new peaks occur at  $476$  and  $546\text{ cm}^{-1}$  associated with the  $E_g$  bending vibration mode and the  $A_{1g}$  stretching vibration mode of  $\text{Ni}^{3+}\text{-O}$  and  $\text{Co}^{3+}\text{-O}$  in  $\text{NiOOH}$  and  $\text{CoOOH}$  [42–44], which correspond to electrooxidation potential of CoNi LDH. Such oxyhydroxides on surface have been demonstrated as the actual active sites for OER, rather than hydroxides [31,45]. The HR-TEM image of CoNi LDH after OER indicates that the electrogenerated  $\text{NiOOH}$  and  $\text{CoOOH}$  are amorphous (Fig. S28a). In the presence of sucrose, the Raman spectra with only two signals at  $462$  and  $520\text{ cm}^{-1}$  of  $\text{Ni}^{2+}\text{-O}$  and  $\text{Co}^{2+}\text{-O}$  are detected throughout the electrochemical potential window (Fig. 3f). Meanwhile, the intensity of peaks of  $\text{Ni}^{2+}\text{-O}$  and  $\text{Co}^{2+}\text{-O}$  gradually increases upon an external voltage of  $1.40\text{ V}$  for SOR, corroborating the escalated disorder in crystallinity [45]. The non-continuous lattice fringes further confirm the escalated disorder of CoNi LDH after SOR (Fig. S28b). It is because that the amorphous CoNi hydroxide is formed by the transformation of amorphous oxyhydroxide. These results indicate that the electrogenerated  $\text{NiOOH}$  and  $\text{CoOOH}$  are reduced to hydroxides by sucrose, confirming a reversible SOR kinetics by reducing the oxyhydroxides with sucrose [39].

The XPS spectra were collected to track the valence state change of the CoNi LDH under different oxidation conditions. As shown in Fig. 3g, two peaks at binding energies of  $779.8\text{ eV}$  for  $\text{Co } 2p_{3/2}$  and  $794.9\text{ eV}$  for  $2p_{1/2}$  appear after OER at  $1.5\text{ V}$ , which are attributed to  $\text{Co}^{3+}$ . Similarly,

these two peaks of  $\text{Ni}^{3+}$  occur in the  $\text{Ni } 2p$  XPS spectra (Fig. S29a). The new peak ascribed to metal-oxygen binding is also observed after OER, further demonstrating the oxidation of CoNi LDH to oxyhydroxides (Fig. S30). Fig. S31 shows that the color of electrode changes from light green to black after OER, owing to the formation of  $\text{NiOOH}$  and  $\text{CoOOH}$ . However, the peaks attributed to  $\text{Co}^{2+}$  and  $\text{Ni}^{2+}$  remain unchanged in the presence of sucrose (Fig. 3h and Fig. S29b). There is no significant variation in the oxygen content of catalyst after SOR (Fig. S32 and Table S4). The color, electronic structure, and morphology (SEM in Fig. S33) of CoNi LDH electrode remain unchanged during the SOR, owing to the reversible redox cycle of  $\text{Ni}^{2+}/\text{Ni}^{3+}$  and  $\text{Co}^{2+}/\text{Co}^{3+}$ .

### 3.4. Hybrid electrolysis for sucrose oxidation and hydrogen production

The sugarcane juice oxidation with economic and environmental benefits offers the opportunity to replace the OER of water electrolysis for hydrogen production. A two-electrode hybrid electrolyser equipped with the CoNi LDH anode and  $\text{CoNiP}_x$  cathode (cobalt/nickel phosphides) was assembled for further demonstration of sugarcane juice oxidation (Fig. 4a). The  $\text{CoNiP}_x$  cathode was prepared by phosphating treatment of CoNi LDH, in view of the low HER activity of CoNi LDH (Fig. S34). Detailed analysis on the  $\text{CoNiP}_x$  cathode was provided in Figs. S35–S37, which confirmed the formations of  $\text{Ni}_2\text{P}$  and  $\text{Co}_2\text{P}$  in  $\text{CoNiP}_x$  electrode. The LSV curves in Fig. S34 demonstrate that  $\text{CoNiP}_x$  exhibits excellent HER activity, with an overpotential of  $180.0\text{ mV}$  to reach a current density of  $100\text{ mA cm}^{-2}$ . The LSV scans in Fig. 4b



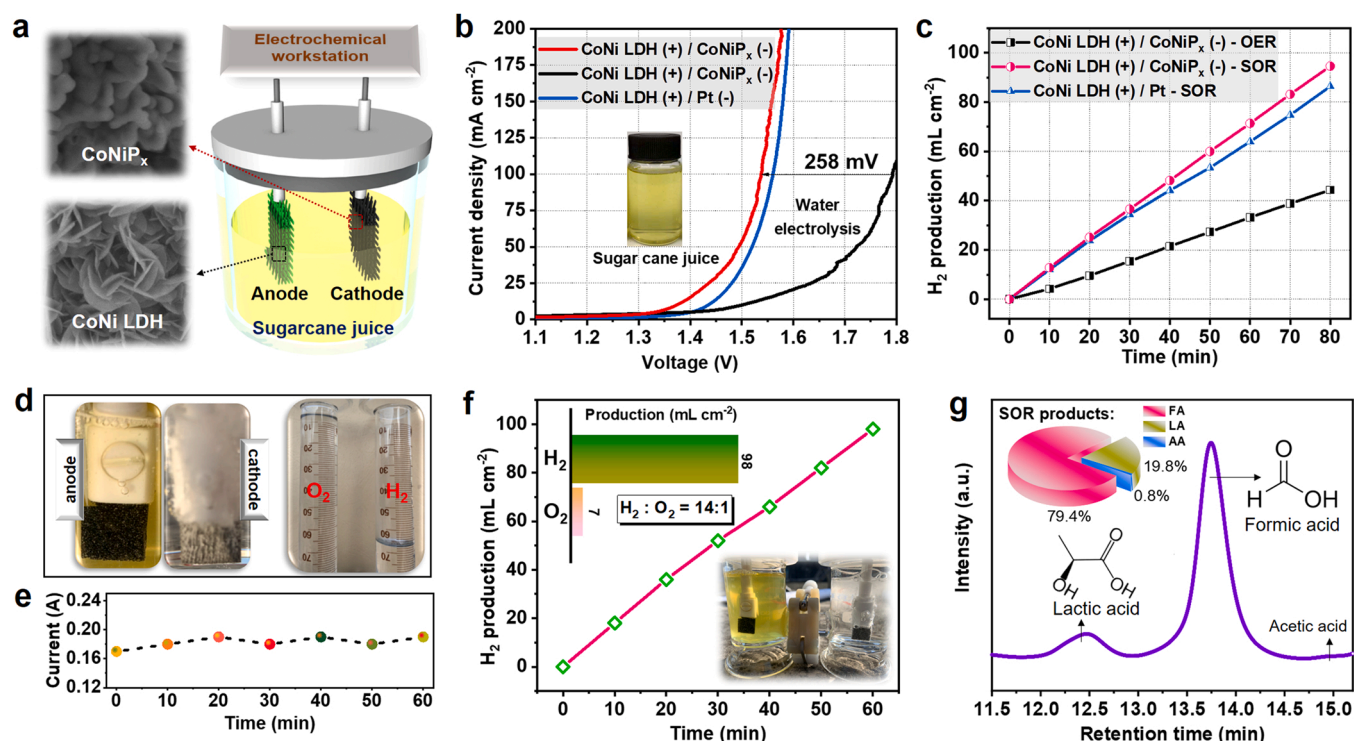


**Fig. 4.** (a) Diagram of the hybrid electrolyser (anode: CoNi LDH; cathode: CoNiP<sub>x</sub> or Pt; electrolyte: sugar cane juice diluted for 10 times in 1 M KOH). (b) The LSV curves and (c) H<sub>2</sub> production of various electrolyser. (d) Photograph of gas collection from anode and cathode in the solar-driven hybrid electrolyser. (e) Full cell current at *versus* reaction times. (f) H<sub>2</sub> and O<sub>2</sub> production rates of the solar-driven hybrid electrolyser. (g) The HPLC traces of FA and LA, inset shows the product selectivities.

validate that the CoNi LDH (+) / CoNiP<sub>x</sub> (-) electrolysis requires a cell voltage of 1.792 V to achieve 100 mA cm<sup>-2</sup> for water splitting. This can be reduced to 1.534 V in presence of sugarcane juice. Such a reduced potential of 258 mV implies the significantly better energy conversion efficiency of hybrid electrolysis. Furthermore, the CoNi LDH (+) / CoNiP<sub>x</sub> (-) system shows the similar current density and the reduced onset potential, compared with that of CoNi LDH (+) / Pt (-). Fig. 4c presents the gas products in the hybrid electrolyser at 1.9 V. The H<sub>2</sub> production rate with sugarcane juice reaches 94.6 mL cm<sup>-2</sup> for 80 min operation, which is 2.13 times higher than that of water electrolysis. No O<sub>2</sub> is produced in such setup owing to the dominance of sugarcane juice oxidation. These results demonstrate that the utility of CoNi-based catalysts as alternative to noble metal catalysts for H<sub>2</sub> generation.

To evaluate the hybrid electrolysis in practical applications, a solar-driven proton exchange membrane (PEM) electrolyser was fabricated with the CoNi LDH anode, CoNiP<sub>x</sub> cathode and an electrolyte containing raw sugarcane juice and 1 M KOH (Fig. S38) [46,47]. A commercial solar panel (maximum power of 3 W, 6 V) was employed to power such hybrid electrolyser during the operation at N 23°8'59.7", E 113°20'46.0" (4–5 pm on 9 March 2022, partially cloudy). The generated O<sub>2</sub> and H<sub>2</sub> products from anode and cathode were collected and measured by water drainage method in Fig. 4d. The solar-driven PEM hybrid electrolysis system with stable current output between 0.17 and 0.19 A was obtained in Fig. 4e, yielding a production rate of H<sub>2</sub> and O<sub>2</sub> at 1.633 and 0.117 mL cm<sup>-2</sup> min<sup>-1</sup>, respectively (Fig. 4f). It is worth noting that only trace amount of O<sub>2</sub> was formed, suggesting that sugarcane juice reactants on anode can minimize OER even at high voltage. The HPLC analysis shows that the product is consisted of mainly FA (79.4 % selectivity) with LA (19.8 %) during sugarcane juice oxidation in Fig. 4g. This PEM system powered by DC power supply was constructed to highlight the prospective way of solar power. When providing 183 mA current to the PEM system, the H<sub>2</sub> and O<sub>2</sub> production rates and liquid products selectivity of DC powered PEM system are close to the

solar-driven system (Fig. S39). These results highlight the effectiveness in lowering operational cost of water electrolysis by solar energy coupled with biomass fuel oxidation.

#### 4. Conclusion

In conclusion, a hybrid electrolyser using raw sugarcane juice was fabricated with the CoNi LDH anode and CoNiP<sub>x</sub> cathode. Owing to thermodynamically favorable sucrose oxidation over oxygen evolution, the potential to reach 100 mA cm<sup>-2</sup> was significantly reduced by 240 mV. A reversible redox cycle of Ni<sup>2+</sup>/Ni<sup>3+</sup> and Co<sup>2+</sup>/Co<sup>3+</sup> in CoNi LDH was visualized by EIS, *in-situ* Raman spectroscopy and *Ex-situ* XPS for the superior sucrose oxidation activity and selectivity toward formic acid. The surface of CoNi LDH retained the hydroxide phase rather than oxyhydroxide during the sucrose oxidation to guarantee its long-term stability. When powered by a 3 W solar panel, our hybrid device enabled a H<sub>2</sub> production rate of 1.633 mL cm<sup>-2</sup> min<sup>-1</sup> and formic acid selectivity of 79.4 % with sugarcane juice oxidation. Our work paves the way towards an efficient hybrid electrolysis system for future biomass valorization and hydrogen production.

#### CRediT authorship contribution statement

**Yunpeng Liu:** Investigation, Data curation, Writing – original draft, Funding acquisition. **Zhongxin Chen:** Data curation, Writing – review & editing. **Yunyi Yang:** Investigation, Data curation. **Ren Zou:** Investigation, Data curation. **Binglu Deng:** Data curation, Formal analysis. **Linlin Zhong:** Writing – review & editing, Supervision. **Kian Ping Loh:** Writing – review & editing, Supervision. **Xinwen Peng:** Writing – review & editing, Supervision, Funding acquisition.

## Declaration of Competing Interest

The authors declare that they have no known competing financial interests or personal relationships that could have appeared to influence the work reported in this paper.

## Data availability

Data will be made available on request.

## Acknowledgements

This work was financially supported by the Guangdong Basic and Applied Basic Research Foundation (No. 2021A1515110622), National Natural Science Foundation of China (No. 31971614), and National Youth Top-notch Talent Support Program (No. x2qsA4210090).

## References

- J. Wang, W. Cui, Q. Liu, Z. Xing, A.M. Asiri, X. Sun, Recent progress in cobalt-based heterogeneous catalysts for electrochemical water splitting, *Adv. Mater.* 28 (2016) 215–230, <https://doi.org/10.1002/adma.201502696>.
- Z.W. Seh, J. Kibsgaard, C.F. Dickens, I. Chorkendorff, J.K. Nørskov, T.F. Jaramillo, Combining theory and experiment in electrocatalysis: insights into materials design, *Science* 355 (2017), eaad4998, <https://doi.org/10.1126/science.aad4998>.
- S. Chu, A. Majumdar, Opportunities and challenges for a sustainable energy future, *Nature* 488 (2012) 294–303, <https://doi.org/10.1038/nature11475>.
- J. Song, C. Wei, Z.F. Huang, C. Liu, L. Zeng, X. Wang, Z.J. Xu, A review on fundamentals for designing oxygen evolution electrocatalysts, *Chem. Soc. Rev.* 49 (2020) 2196–2214, <https://doi.org/10.1039/c9cs00607a>.
- J. Luo, J.H. Im, M.T. Mayer, M. Schreier, M.K. Nazeeruddin, N.G. Park, S.D. Tilley, H.J. Fan, M. Gratzel, Water photolysis at 12.3% efficiency via perovskite photovoltaics and earth-abundant catalysts, *Science* 345 (2014) 1593–1596, <https://doi.org/10.1126/science.1258307>.
- A. Berger, R.A. Segalman, J. Newman, Material requirements for membrane separators in a water-splitting photoelectrochemical cell, *Energy Environ. Sci.* 7 (2014) 1468–1476, <https://doi.org/10.1039/c3ee43807d>.
- B. You, X. Liu, N. Jiang, Y. Sun, A general strategy for decoupled hydrogen production from water splitting by integrating oxidative biomass valorization, *J. Am. Chem. Soc.* 138 (2016) 13639–13646, <https://doi.org/10.1021/jacs.6b07127>.
- C.W. Anson, S.S. Stahl, Mediated fuel cells: soluble redox mediators and their applications to electrochemical reduction of O<sub>2</sub> and oxidation of H<sub>2</sub>, alcohols, biomass, and complex fuels, *Chem. Rev.* 120 (2020) 3749–3786, <https://doi.org/10.1021/acs.chemrev.9b00717>.
- W.J. Liu, Z. Xu, D. Zhao, X.Q. Pan, H.C. Li, X. Hu, Z.Y. Fan, W.K. Wang, G.H. Zhao, S. Jin, G.W. Huber, H.Q. Yu, Efficient electrochemical oxidation of glucaric acid and H<sub>2</sub> via glucose electrolysis, *Nat. Commun.* 11 (2020) 265, <https://doi.org/10.1038/s41467-019-14157-3>.
- Y. Lu, T. Liu, C.L. Dong, C. Yang, L. Zhou, Y.C. Huang, Y. Li, B. Zhou, Y. Zou, S. Wang, Tailoring competitive adsorption sites by oxygen-vacancy on cobalt oxides to enhance the electrooxidation of biomass, *Adv. Mater.* 34 (2021), 2107185, <https://doi.org/10.1002/adma.202107185>.
- L. Sha, K. Ye, J. Yin, K. Zhu, K. Cheng, J. Yan, G. Wang, D. Cao, In situ grown 3D hierarchical MnCo<sub>2</sub>O<sub>4.5</sub>@Ni(OH)<sub>2</sub> nanosheet arrays on Ni foam for efficient electrocatalytic urea oxidation, *Chem. Eng. J.* 381 (2020), 122603, <https://doi.org/10.1016/j.cej.2019.122603>.
- J. Ma, Y. Li, D. Jin, X. Yang, G. Jiao, K. Liu, S. Sun, J. Zhou, R. Sun, Reasonable regulation of carbon/nitride ratio in carbon nitride for efficient photocatalytic reforming of biomass-derived feedstocks to lactic acid, *Appl. Catal. B Environ.* 299 (2021), 120698, <https://doi.org/10.1016/j.apcatb.2021.120698>.
- R. Li, K. Xiang, Z. Peng, Y. Zou, S. Wang, Recent advances on electrolysis for simultaneous generation of valuable chemicals at both anode and cathode, *Adv. Energy Mater.* 11 (2021), 2102292, <https://doi.org/10.1002/aenm.202102292>.
- T. Wang, Z. Huang, T. Liu, L. Tao, J. Tian, K. Gu, X. Wei, P. Zhou, L. Gan, S. Du, Y. Zou, R. Chen, Y. Li, X.Z. Fu, S. Wang, Transforming electrocatalytic biomass upgrading and hydrogen production from electricity input to electricity output, *Angew. Chem. Int. Ed.* 61 (2022), e202115636, <https://doi.org/10.1002/anie.202115636>.
- Z. Chen, C. Liu, X. Zhao, H. Yan, J. Li, P. Lyu, Y. Du, S. Xi, K. Chi, X. Chi, H. Xu, X. Li, W. Fu, K. Leng, S.J. Pennycook, S. Wang, K.P. Loh, Promoted glycerol oxidation reaction in an interface-confined hierarchically structured catalyst, *Adv. Mater.* 31 (2019), 1804763, <https://doi.org/10.1002/adma.201804763>.
- X. Bai, Q. Hou, H. Qian, Y. Nie, T. Xia, R. Lai, G. Yu, M. Laiq Ur Rehman, H. Xie, M. Ju, Selective oxidation of glucose to gluconic acid and glucaric acid with chlorin e6 modified carbon nitride as metal-free photocatalyst, *Appl. Catal. B Environ.* 303 (2022), 120895, <https://doi.org/10.1016/j.apcatb.2021.120895>.
- Y. Li, X. Wei, L. Chen, J. Shi, M. He, Nickel-molybdenum nitride nanoplate electrocatalysts for concurrent electrolytic hydrogen and formate productions, *Nat. Commun.* 10 (2019) 5335, <https://doi.org/10.1038/s41467-019-13375-z>.
- C. Dang, W. Yang, J. Zhou, W. Cai, Porous Ni-Ca-Al-O Bi-functional catalyst derived from layered double hydroxide intercalated with citrate anion for sorption-enhanced steam reforming of glycerol, *Appl. Catal. B Environ.* 298 (2021), 120547, <https://doi.org/10.1016/j.apcatb.2021.120547>.
- A.J. Wacławowski, P.M. Sato, C.G. Lemke, P.H. Moore, G.M. Souza, Sugarcane for bioenergy production: an assessment of yield and regulation of sucrose content, *Plant Biotechnol. J.* 8 (2010) 263–276, <https://doi.org/10.1111/j.1467-7652.2009.00491.x>.
- Y. Jugwanth, Y. Sewsynker-Sukai, E.B. Gueguim Kana, Valorization of sugarcane bagasse for bioethanol production through simultaneous saccharification and fermentation: optimization and kinetic studies, *Fuel* 262 (2020), 116552, <https://doi.org/10.1016/j.fuel.2019.116552>.
- W. Antonio Bizzo, P.C. Lenço, D.J. Carvalho, J.P.S. Veiga, The generation of residual biomass during the production of bio-ethanol from sugarcane, its characterization and its use in energy production, *Renew. Sustain. Energy Rev.* 29 (2014) 589–603, <https://doi.org/10.1016/j.rser.2013.08.056>.
- Q. Dong, M. Li, M. Sun, F. Si, Q. Gao, X. Cai, Y. Xu, T. Yuan, S. Zhang, F. Peng, Y. Fang, S. Yang, Phase-controllable growth Ni<sub>x</sub>P<sub>y</sub> modified CdS@Ni<sub>3</sub>S<sub>2</sub> electrodes for efficient electrocatalytic and enhanced photoassisted electrocatalytic overall water splitting, *Small Methods* 5 (2021), 2100878, <https://doi.org/10.1002/smt.202100878>.
- R. Yang, Y. Zhou, Y. Xing, D. Li, D. Jiang, M. Chen, W. Shi, S. Yuan, Synergistic coupling of CoFe-LDH arrays with NiFe-LDH nanosheet for highly efficient overall water splitting in alkaline media, *Appl. Catal. B Environ.* 253 (2019) 131–139, <https://doi.org/10.1016/j.apcatb.2019.04.054>.
- H. Luo, B. Wang, T. Liu, F. Jin, R. Liu, C. Xu, C. Wang, K. Ji, Y. Zhou, D. Wang, S. Dou, Hierarchical design of hollow Co-Ni LDH nanocages strung by MnO<sub>2</sub> nanowire with enhanced pseudocapacitive properties, *Energy Storage Mater.* 19 (2019) 370–378, <https://doi.org/10.1016/j.ensm.2018.10.016>.
- H. Chen, L. Hu, M. Chen, Y. Yan, L. Wu, Nickel-cobalt layered double hydroxide nanosheets for high-performance supercapacitor electrode materials, *Adv. Funct. Mater.* 24 (2014) 934–942, <https://doi.org/10.1002/adfm.201301747>.
- L. Wan, D. Chen, J. Liu, Y. Zhang, J. Chen, M. Xie, C. Du, Construction of FeNiP@CoNi-layered double hydroxide hybrid nanosheets on carbon cloth for high energy asymmetric supercapacitors, *J. Power Sources* 465 (2020), 228293, <https://doi.org/10.1016/j.jpowsour.2020.228293>.
- D. Zhou, Z. Cai, X. Lei, W. Tian, Y. Bi, Y. Jia, N. Han, T. Gao, Q. Zhang, Y. Kuang, J. Pan, X. Sun, X. Duan, NiCoFe-layered double hydroxides/N-doped graphene oxide array colloid composite as an efficient bifunctional catalyst for oxygen electrocatalytic reactions, *Adv. Energy Mater.* 8 (2018), 1701905, <https://doi.org/10.1002/aenm.201701905>.
- G. Jia, Y. Hu, Q. Qian, Y. Yao, S. Zhang, Z. Li, Z. Zou, Formation of hierarchical structure composed of (Co/Ni)Mn-LDH nanosheets on MWCNT backbones for efficient electrocatalytic water oxidation, *ACS Appl. Mater. Interfaces* 8 (2016) 14527–14534, <https://doi.org/10.1021/acsami.6b02733>.
- R. Ma, J. Liang, K. Takada, T. Sasaki, Topochemical synthesis of Co-Fe layered double hydroxides at varied Fe/Co ratios: unique intercalation of triiodide and its profound effect, *J. Am. Chem. Soc.* 133 (2011) 613–620, <https://doi.org/10.1021/ja1087216>.
- Q. Zhou, Y. Chen, G. Zhao, Y. Lin, Z. Yu, X. Xu, X. Wang, H.K. Liu, W. Sun, S. X. Dou, Active-site-enriched iron-doped nickel/cobalt hydroxide nanosheets for enhanced oxygen evolution reaction, *ACS Catal.* 8 (2018) 5382–5390, <https://doi.org/10.1021/acscatal.8b01332>.
- A. Moysiadou, S. Lee, C.S. Hsu, H.M. Chen, X. Hu, Mechanism of oxygen evolution catalyzed by cobalt oxyhydroxide: cobalt superoxide species as a key intermediate and dioxygen release as a rate-determining step, *J. Am. Chem. Soc.* 142 (2020) 11901–11914, <https://doi.org/10.1021/jacs.0c04867>.
- M. Kuang, P. Han, Q. Wang, J. Li, G. Zheng, CuCo hybrid oxides as bifunctional electrocatalyst for efficient water splitting, *Adv. Funct. Mater.* 26 (2016) 8555–8561, <https://doi.org/10.1002/adfm.201604804>.
- R. Zhang, S. Jiang, Y. Rao, S. Chen, Q. Yue, Y. Kang, Electrochemical biomass upgrading on CoOOH nanosheets in a hybrid water electrolyzer, *Green Chem.* 23 (2021) 2525–2530, <https://doi.org/10.1039/d0gc04157b>.
- S. Anantharaj, S. Noda, M. Driess, P.W. Menezes, The pitfalls of using potentiodynamic polarization curves for tafel analysis in electrocatalytic water splitting, *ACS Energy Lett.* 6 (2021) 1607–1611, <https://doi.org/10.1021/acsenenergylett.1c00608>.
- R. Vinu, L.J. Broadbelt, A mechanistic model of fast pyrolysis of glucose-based carbohydrates to predict bio-oil composition, *Energy Environ. Sci.* 5 (2012) 9808, <https://doi.org/10.1039/c2ee22784c>.
- Y. Liu, R. Zou, B. Qin, J. Gan, X. Peng, Energy-efficient monosaccharides electrooxidation coupled with green hydrogen production by bifunctional Co<sub>9</sub>S<sub>8</sub>/Ni<sub>3</sub>S<sub>2</sub> electrode, *Chem. Eng. J.* 446 (2022), 136950, <https://doi.org/10.1016/j.cej.2022.136950>.
- H.Y. Wang, S.F. Hung, H.Y. Chen, T.S. Chan, H.M. Chen, B. Liu, In operando identification of geometrical-site-dependent water oxidation activity of spinel Co<sub>3</sub>O<sub>4</sub>, *J. Am. Chem. Soc.* 138 (2016) 36–39, <https://doi.org/10.1021/jacs.5b10525>.
- Y. Lu, C.L. Dong, Y.C. Huang, Y. Zou, Z. Liu, Y. Liu, Y. Li, N. He, J. Shi, S. Wang, Identifying the geometric site dependence of spinel oxides for the electrooxidation of 5-hydroxymethylfurfural, *Angew. Chem. Int. Ed.* 59 (2020) 19215–19221, <https://doi.org/10.1002/anie.202007767>.
- Y. Zhang, B. Zhou, Z. Wei, W. Zhou, D. Wang, J. Tian, T. Wang, S. Zhao, J. Liu, L. Tao, S. Wang, Coupling glucose-assisted Cu(I)/Cu(II) redox with electrochemical hydrogen production, *Adv. Mater.* 33 (2021), 2104791, <https://doi.org/10.1002/adma.202104791>.



- [40] M.W. Louie, A.T. Bell, An investigation of thin-film Ni-Fe oxide catalysts for the electrochemical evolution of oxygen, *J. Am. Chem. Soc.* 135 (2013) 12329–12337, <https://doi.org/10.1021/ja405351s>.
- [41] L. Chen, H. Wang, X. Shen, Y. Zhang, D. Li, C. Duan, A novel route for the generation of Co/CoZn/CoNi layered double hydroxides at ambient temperature, *Inorg. Chem. Front.* 6 (2019) 1415–1421, <https://doi.org/10.1039/C9QI00340A>.
- [42] P. Zhang, X. Sheng, X. Chen, Z. Fang, J. Jiang, M. Wang, F. Li, L. Fan, Y. Ren, B. Zhang, B.J.J. Timmer, M.S.G. Ahlquist, L. Sun, Paired electrocatalytic oxygenation and hydrogenation of organic substrates with water as the oxygen and hydrogen source, *Angew. Chem. Int. Ed.* 58 (2019) 9155–9159, <https://doi.org/10.1002/anie.201903936>.
- [43] X. Deng, G.Y. Xu, Y.J. Zhang, L. Wang, J. Zhang, J.F. Li, X.Z. Fu, J.L. Luo, Understanding the roles of electrogenerated  $\text{Co}^{3+}$  and  $\text{Co}^{4+}$  in selectivity-tuned 5-hydroxymethylfurfural oxidation, *Angew. Chem. Int. Ed.* 60 (2021) 20535–20542, <https://doi.org/10.1002/anie.202108955>.
- [44] Y.J. Wu, J. Yang, T.X. Tu, W.Q. Li, P.F. Zhang, Y. Zhou, J.F. Li, J.T. Li, S.G. Sun, Evolution of cationic vacancy defects: a motif for surface restructuring of OER precatalyst, *Angew. Chem. Int. Ed.* 60 (2021) 26829–26836, <https://doi.org/10.1002/anie.202112447>.
- [45] H. Sun, L. Chen, Y. Lian, W. Yang, L. Lin, Y. Chen, J. Xu, D. Wang, X. Yang, M. H. Rummerli, J. Guo, J. Zhong, Z. Deng, Y. Jiao, Y. Peng, S. Qiao, Topotactically transformed polygonal mesopores on ternary layered double hydroxides exposing under-coordinated metal centers for accelerated water dissociation, *Adv. Mater.* 32 (2020), 2006784, <https://doi.org/10.1002/adma.202006784>.
- [46] H. Zhao, D. Lu, J. Wang, W. Tu, D. Wu, S.W. Koh, P. Gao, Z.J. Xu, S. Deng, Y. Zhou, B. You, H. Li, Raw biomass electroreforming coupled to green hydrogen generation, *Nat. Commun.* 12 (2021) 2008, <https://doi.org/10.1038/s41467-021-22250-9>.
- [47] B. Qin, Y. Li, H. Wang, G. Yang, Y. Cao, H. Yu, Q. Zhang, H. Liang, F. Peng, Efficient electrochemical reduction of  $\text{CO}_2$  into CO promoted by sulfur vacancies, *Nano Energy* 60 (2019) 43–51, <https://doi.org/10.1016/j.nanoen.2019.03.024>.